DOI: https://doi.org/10.2138/am-2023-9254. http://www.minsocam.org/

Revision 1

Word Count: 9582

Interpreting Mineral Deposit Genesis Classification with Decision Maps: A Case Study Using Pyrite Trace Elements

Yu Wang[a,b], Kun-Feng Qiu[a,*], Alexandru C. Telea[b], Zhao-Liang Hou[a,c,*], Tong Zhou[a], Yi-Wei Cai[a], Zheng-Jiang Ding[d], Hao-Cheng Yu[a], Jun Deng[a,e]

[a] Frontiers Science Center for Deep-time Digital Earth, State Key Laboratory of Geological Processes and Mineral Resources, School of Earth Sciences and Resources, China University of Geosciences, Beijing 100083, China

[b] Department of Information and Computing Sciences, Utrecht University, Utrecht, 3584 CC, Netherlands

[c] Department of Geology, University of Vienna, Althanstraße 14, Vienna, 1090, Austria

[d] Ministry of Natural Resources Technology Innovation Center for Deep Gold Resources Exploration and Mining, No. 6 Geological Team of Shandong Provincial Bureau of Geology and Mineral Resources, Weihai, Shandong 264209, China

[e] Geological Research Institute of Shandong Gold Group Co., Ltd, Jinan, 250013, China

* Corresponding author: Kun-Feng Qiu (kunfengqiu@qq.com), ORCID: 0000-0002-3185-9446; Zhao-Liang Hou (zhaolianghou@163.com), OCRID: 0000-0003-4937-2940.

Abstract

Machine learning improves geochemistry discriminant diagrams in classifying mineral deposit genetic types. However, the increasingly recognized 'black box' property of machine learning has been hampering the transparency of complex data analysis, leading to the challenge in deep geochemical interpretation. To address the issue, we revisited pyrite trace elements and propose to use 'Decision Map', a cutting-edge visualization technique for machine learning. This technique reveals mineral deposit classifications by visualizing the 'decision boundaries' of high-dimensional data, a concept crucial for model interpretation, active learning, and domain adaptation. In the context of geochemical data classification, it enables geologists to understand the relationship between geo-data and decision boundaries, assess prediction certainty, and observe the data distribution trends. This bridges the gap between the insightful properties of traditional discriminant diagrams and the high-dimensional efficiency of modern machine learning. Using pyrite trace element data, we construct a decision map for mineral deposit type classification, which maintains the accuracy of machine learning while adding valuable visualization insight. Additionally, we demonstrate two applications of decision maps. First, we show how decision maps can help resolve the genetic type dispute of a deposit whose data was not used in training the models. Second, we demonstrate how the decision maps can help understand the model, which further helps find indicator elements of pyrite. The recommended indicator elements by decision maps are consistent with geologists' knowledge. This study confirms the decision map's effectiveness in interpreting mineral genetic type classification problems. In geochemistry classification, it marks a shift from conventional machine learning to a visually insightful approach, thereby enhancing the geological understanding derived from the model. Furthermore, our work implies that decision maps could be applicable to diverse classification challenges in geosciences.

Keywords:

Decision map; Mineral deposit genesis; Machine learning classification; Pyrite trace element; Discriminant diagrams

Introduction

The accelerating pace of data generation and computational power, coupled with the burgeoning interest of geoscientists in machine learning, is leading to significant breakthroughs in the applications and discoveries in Geosciences (Petrelli and Perugini, 2016; Bergen et al., 2019; Karpatne et al., 2019, Petrelli 2021; Hou et al., 2024). The data-driven study in geosciences essentially aims at digging deep information from complex/huge data sets, rather than merely and simply producing classification or prediction models. The 'black box' nature of machine models, however, hinders our understanding of decision-making processes during machine learning (Lipton, 2018; Carvalho et al., 2019; Molnar, 2020). Although pioneering explorations on the transparency of the working pathway of machine learning have emphasized the significance of the interpretability machine learning model (Lipton, 2018; Carvalho et al., 2019; Molnar, 2020; Yuang et al., 2021), such work is lacking in the classification of mineral deposit genetic environments.

Understanding the mineral deposit genetic environments is important to explore the physio-chemical conditions that are responsible for the ore formation (Deng et al., 2016, 2020a, b; Qiu et al., 2024b). To improve the precision of the ore deposit classification environment, with a transparent and interpretable machine learning approach, we introduce and apply the innovative visualization technique of *decision map*, developed by Rodrigues et al. (2019) and Oliveira et

DOI: https://doi.org/10.2138/am-2023-9254. http://www.minsocam.org/

al. (2022). The visualization method reveals how various machine learning classifiers function by conducting dimensionality reduction and providing a clear, visual representation of decision zones, with each zone signifying a different inferred class (Rodrigues et al., 2019). This compelling visualization approach fosters a better understanding of the classification process.

We underscore the potency of decision maps within a fundamental geological domain: the genesis of mineral deposits. The dwindling supply of near-surface ore deposits necessitates deeper exploration (Gregory et al., 2019). The ability to recognize the type of mineralization present in a given context can offer critical insights, thus streamlining exploration efforts and minimizing associated costs (Gregory et al., 2019). Trace elements measured in specific minerals, such as quartz, pyrite, apatite, and zircon, can serve as unique identifiers for understanding their genesis, revealing types of minerals deposits and host rock genetic environments (Belousova et al., 2002b; Chew et al., 2012; Rusk, 2012; O'Sullivan et al., 2020; Wang et al., 2021; Zhong et al., 2021; Zhu et al., 2022; Zhou et al., 2023)

Classification of mineral deposits environments has traditionally been studied using visual tools, including discriminant diagrams (Pearce & Cann, 1973; Bralia et al., 1979; Belousova et al., 2002a, 2002b; Rusk, 2012; Li et al., 2015; Breiter et al., 2020, Zhou et al., 2022), and, more recently, machine learning-assisted approaches (Petrelli & Perugini, 2016; Gregory et al., 2019; Wang et al., 2021; Zhong et al., 2021; Liu et al., 2023; Qiu et al., 2024c). However, striking a balance between visual interpretability and accuracy is still a challenge. There have also been some attempts of using machine learning to optimize geochemistry discriminant diagrams (O'Sullivan et al., 2020; Wang et al., 2022). Such applications improve the quality of the patterns depicted by the diagrams but still do not take full advantage of high-dimensional information. Here, decision maps come to the fore, combining the high-accuracy of machine learning models with visual accessibility to decision boundaries, greatly promoting transparency and interpretability. This study represents the first application of visualization to elucidate machine learning classification in mineral deposit genetic types, highlighting the paramount role of visualization techniques in modern data interpretation and decision-making.

Here, our contributions straddle both information visualization and mineralogy domains: (1) We offer a unique pyrite trace elements dataset comprising six genetic populations. (2) We illuminate the added value of the decision map technique in deciphering the machine learning classification results, opening up new avenues for using decision maps. (3) We introduce a method that seamlessly blends the merits of traditional 2D discriminant diagrams (visual interpretability) and machine learning methods (high accuracy), providing a robust framework for mineral genesis classification problems. This blend of visualization and machine learning underlines the evolving landscape of data science, championing transparency and interpretability.

Background

Machine learning classifiers for mineral genetic type classification

Machine learning is the emerging approach to solving geochemistry data classification problems (Gregory et al., 2019; O'Sullivan et al., 2020; Petrelli & Perugini, 2016; Wang et al., 2021). We start by introducing a few notations. Let $D = \{\boldsymbol{x}_i\} \subset \mathbb{R}^n$, $1 \leq i \leq N$, be a dataset of n-dimensional data points $\boldsymbol{x}_i = \{x_i^1, x_i^2, \cdots, x_i^n\}$ with corresponding labels $y_i \in C$, where C is the set of classes. Let $\boldsymbol{x}^j = \{x_1^j, x_2^j, \cdots, x_N^j\}, 1 \leq j \leq n$, be the j-th feature of D. Thus, D can be seen as a table with N rows (samples) and n columns (dimensions or features), and $\boldsymbol{y} = \{y_1, y_2, \cdots, y_N\}$ is the corresponding label vector. Simply put, given a dataset D, a machine learning classifier constructs a function $f : \mathbb{R}^n \rightarrow C$ so that $f(\boldsymbol{x}_i) = y_i$ for ideally all $\boldsymbol{x}_i \in D_t$, where $D_t \subseteq D$ is so the called training set. After training, one uses the model f to infer labels of unseen points $\mathbf{x}_i$. In the present work, we tested different machine learning classification algorithms, including Logistic Regression (Cox, 1958), Support Vector Machines (SVM) (Cortes & Vapnik, 1995), Random Forests (Breiman, 2001), and Neural Networks. They represent distinct families of algorithms: Logistic Regression is a linear classification model; SVM stands as a maximum margin classifier; Random Forest embodies an ensemble method; and Neural Network signifies deep learning. Crucially, these classifiers are frequently examined in mineral classification studies (Gregory et al., 2019; Zhong et al., 2021). This frequent examination not only enables a thorough comparative analysis but also underscores the relevance and robustness of our conclusions within the machine learning applications in geosciences.

Although machine learning methods efficiently process high-dimensional data, enabling the accurate identification of numerous mineral classes with minimal human effort, they often face criticism for their black-box nature, which provides limited insight into the reasoning behind classifications. Our work aims to reveal the black box by extending machine learning classifiers with decision maps, which is elaborated in the following section.

Decision Maps

A decision map is a visualization technique designed to display the decision boundaries of classifiers. A decision boundary, in essence, is a surface that segregates high-dimensional data points $\mathbf{x}_i \in \mathbb{R}^n$ into distinct regions or decision zones. Within each zone, all points receive the same label from the classifier f. Analyzing these zones provides insights into the classifier's behavior, such as pinpointing misclassification issues based on how labeled samples are distributed near decision boundaries and understanding the classifier's generalization based on the distribution of unlabeled samples.

Historically, visualizing these decision zones was a challenge. To address this, Rodrigues et al. (2018, 2019) proposed Decision Boundary Map (DBM), which can visualize decision boundaries for *any* selected classifier. After a classifier f is trained on a high-dimensional dataset D, their method projects D to a 2D scatterplot $P(D) = \{P(\boldsymbol{x}) \mid \boldsymbol{x} \in D\}$. This is done using dimensionality reduction, or projection, methods P such as PCA or t-SNE (Van der Maaten & Hinton, 2008). Next, every pixel p in the 2D bounding box of $P(D)$ is inversely projected to R^n to create synthetic data points $P^{-1}(\mathbf{p})$. These are then classified by f and their corresponding pixels p are colored by the assigned class labels $f(P^{-1}(\mathbf{p}))$. To construct decision maps, one thus needs to have a projection method P: $\mathbb{R}^n \rightarrow \mathbb{R}^2$ and its inverse $P^{-1} : \mathbb{R}^2 \rightarrow \mathbb{R}^n$. Unavoidably, both the direct and inverse projections P and P^{-1} introduce errors – that is, in general, P^{-1} is not an exact inverse of P, i.e., $P^{-1}(P(\mathbf{x})) \neq \mathbf{x}$ for several data points $\mathbf{x}$. However, such errors can be evaluated by metrics (see next section).

To compute the P and P^{-1} pair, Espadoto et al. (2021) proposed Self-Supervised Network Projections (SSNP), a deep learning method that jointly addresses P, P^{-1}, and data clustering. Using SSNP, Oliveira et al. (2022) proposed Supervised Decision Boundary Map (SDBM), a method that increases both the speed and quality of the original DBM method. Thus, SDBM was employed to construct decision maps for all the following experiments.

Methods

Dataset collection

The dataset used in this study is a compilation of published pyrite trace elements datasets. Pyrite is a ubiquitous mineral in the crust. Appearing in various mineral deposit types, its trace elements can fingerprint its forming environments

DOI: https://doi.org/10.2138/am-2023-9254. http://www.minsocam.org/

(Belousov et al., 2016; Zhong et al., 2021). In this study, we compiled a dataset with 3571 pyrite LA-ICP-MS analyses from different origins, including Ni-Cu/platinum group element deposits (Ni-Cu-PGE, igneous deposits), porphyry deposits, orogenic deposits, Carlin-type Au, volcanic-hosted massive sulfide (VHMS) deposits, and barren sedimentary pyrite. Eleven trace elements (Co, Ni, Cu, Zn, Se, As, Ag, Sb, Au, Bi, Pb) are selected as features, or dimensions, for our study. Each trace element was measured in parts per million (ppm) and these measurements were used to train machine learning classifiers which are next explored using the decision map. Detailed information on the compiled dataset is shown in Table 1, including the used data sources.

Workflow

After assembling the dataset to be used for classification, the following workflow was conducted: data preprocessing, SDBM training, search for best classifiers, map building, and evaluation.

Metrics. To select the best classifier-decision map pair, we use the following three metrics, which are core metrics for decision map evaluations (Wang et al., 2023).

Classifier accuracy *ACCc*, computed traditionally, is the fraction of correct predictions in a high-dimensional dataset and its respective labels. It is defined as

$$ACC_C = \frac{|\{\boldsymbol{x}_i \in D \mid C(\boldsymbol{x}_i) = f(\boldsymbol{x}_i)\}|}{|D|}, \qquad (1)$$

This is the peer-reviewed, final accepted version for American Mineralogist, published by the Mineralogical Society of America.
The published version is subject to change. Cite as Authors (Year) Title. American Mineralogist, in press.
DOI: https://doi.org/10.2138/am-2023-9254. http://www.minsocam.org/

where $|\cdot|$ denotes the size of a set, and D is the sample set (with labels in C) used for evaluation.

Map accuracy ACC_M is the proportion of correctly positioned data points in the decision zones for a given dataset. It is defined as

$$ACC_M = \frac{|\{\boldsymbol{x}_i \in D \mid C(\boldsymbol{x}_i) = f(P^{-1}(P(\boldsymbol{x}_i)))\}|}{|D|}. \quad (2)$$

Data consistency *Cons* measures the proportion of samples that retain their predicted labels, as determined by the classifier f, after the direct-inverse projection cycle. It is defined as

$$Cons = \frac{\left|\left\{\boldsymbol{x}_i \in D \mid f\left(P^{-1}\left(P(\boldsymbol{x}_i)\right)\right) = f(\boldsymbol{x}_i)\right\}\right|}{|D|}. \quad (3)$$

Data preprocessing. The data were processed by the following steps:

Data missing value imputation: Unless not measured, missing values in the input dataset indicate analyses below detection limits. Missing values were set to half the detection limit to keep the data distribution.

Data transformation: Normality of the features is desired for downstream machine learning model training. Trace elements in minerals are lognormal distributed. A power transformation (Yeo & Johnson, 2000), given by

$$T\left(x_i^j\right) = log_{10}\left(x_i^j + 1\right) \quad (4)$$

was applied to each sample i in each dimension j to obtain this desired normality.

Data splitting: The whole dataset was randomly split into a training set D_t (80%) and a test set D_T (20%) by stratified sampling while keeping each class's proportions. D_t was used to train the classifier and SDBM, while the D_T was used to evaluate the performance of the classifier, the quality of the computed SDBM, and finally the classifier-SDBM combination.

Oversampling: Decision functions would favor the class with the larger number of samples as our dataset is unbalanced. To correct this, the Synthetic Minority Oversampling Technique (SMOTE) (Chawla et al., 2002) was applied to D_t. Note that this does not affect our final results since we split D_T before oversampling.

Optimal decision boundary map construction. In the following, we describe the pipeline we use to construct the optimal decision map. The workflow is summarized in Figure 1.

SDBM training: Building decision maps followed the SDBM pipeline (Oliveira et al., 2022), except that we trained SSNP, the technique used for constructing P and P^{-1} before training the classifier. This was needed because our aim next was to search for the best classifier among candidates evaluated using the *same* SSNP instance.

Classifier search: Four classifiers were evaluated by stratified K-fold cross-validation on the training set using the metrics described by Equations 1-3. These classifiers included Logistic Regression, SVM (with an RBF kernel), Random

Forests (200 estimators), and a Neural Network (3 hidden layers of 100 units each). All these models were constructed using scikit-learn (Pedregosa et al., 2011). The classifier with the highest cross-validation scores (Equations 1-3) was selected and retrained to build the final decision map.

Map building: We created the final decision map following the procedure detailed in Oliveira et al. (2022). The decision map resolution was set to 300^2 pixels. Pixels $\mathbf{p}$ were colored by the class value $f(P^{-1}(\mathbf{p}))$. To represent confidence levels (prediction probability of f) on the decision map, we adjusted the brightness of each pixel. Pixels $\mathbf{p}$ in areas with lower confidence, typically near the boundaries where decisions change, are shown in darker shades. In contrast, $\mathbf{p}$ in high confidence areas, well inside a clear decision region, are shown in brighter shades. The visual approach allows users to quickly see where the model's predictions are more or less certain.

Evaluation: The retrained classifier and SDBM were finally evaluated on D_T with the metrics in Equations 1-3.

Results

The results of the classifier search are shown in Table 2. Random forests got the highest ACC_C but the lowest ACC_M, which can be considered a poor generalization; SVM ranked third in ACC_C and first in both ACC_M and *Cons*; Neural Network had slightly lower results than Random forests for all three considered metrics; Logistic regression did not obtain competitive results in classifier accuracy compared to the other three models, its ACC_C being 0.09 lower than the penultimate one (SVM). Based on all three metrics, we selected SVM as the best classifier for building the decision map. The resulting map of pyrite classification built for SVM is shown in Fig. 2 with samples of both the training and test set plotted. Test set samples are dots with black outlines; training set samples are dots without outlines. We see that most samples fall within their respective decision zones, which already indicates a good classification performance.

For the evaluation on the test set D_T, SVM got an overall accuracy ACC_C = 0.91 (Equation 1), while the SDBM got an overall accuracy ACC_M = 0.88 (Equation 2) and a consistency *Cons* = 0.90 (Equation 3). The confusion matrices of both the SVM and the SDBM are shown in Fig. 3. ACC_M is 0.03 lower than ACC_C. This minor discrepancy, which is nearly uniform across all classes, suggests that the SDBM's (inverse) projection process (P and P^{-1}) introduces a minimal classification error for the SVM. This negligible drop of accuracy indicates that the SDBM faithfully represents the actual classifier's decision boundaries.

Applications

We next present two applications of the decision maps to show their added-value in classifier construction and analysis. First, we demonstrate how decision maps work on samples from unseen locations and show their added-value in conjunction with regular machine learning methods. Second, we demonstrate how decision maps can help data exploration and model explanation.

Unseen location application examples

Case Study: Analysis of the Zaozigou Gold Deposit. The trained classifier and its decision map were applied to data of pyrite trace elements from a new location – the Zaozigou gold deposit, which is unseen by the models. Zaozigou is the largest gold deposit (118t Au) that is under operation in the Gannan area in the Triassic West Qinling orogenic belt in China (Qiu et al., 2020). Pyrite is the main gold-bearing mineral in this deposit, and its trace elements can be used to identify the physicochemical conditions of gold mineralization (Yu et al., 2022a; Qiu et al., 2023). The genetic classification however is still in debate, which hinders our understanding for ore formation and future explanation strategy (Qiu et al., 2020, 2024a). Sui et al. (2020) considered that the Zaozigou deposit is a reduced intrusion-related gold system (magmatic); Qiu et al. (2020) and Yu et al. (2022b) argued that this deposit is best classified as an epizonal orogenic Au-Sb deposit (metamorphic hydrothermal) based on in situ monazite geochronology.

The fine-labeled pyrite trace element data from Sui et al. (2020) was analyzed using the trained classifier and decision map. The pyrites are categorized into three types: (1) Py1a: pyrites in sedimentary rocks, (2) Py1b: pyrites in dike-hosted ores, and (3) Py2: pyrite grains in quartz-sulfide-ankerite veinlets. We believe that this example demonstrates our new approach's utility in solving real scientific problems.

Classifying Pyrite from Zaozigou. The data from the Zaozigou deposits yield results in two parts: the regular machine learning classifier (SVM) results (Table 3) and the decision map (SDBM) results (Table 4, Fig. 4). (1) For the samples labeled Py1a (pyrite sedimentary rocks), the SVM classified 56% of them as orogenic pyrite and 44% as pyrite in Carlin-type deposits; on the decision map, 46% of these samples were plotted in the sedimentary zone, 39% in the orogenic zone, and 15% in the Carlin zone. (2) For samples labeled Py1b (dike-hosted ores), most are classified as orogenic (94% and 84% for SVM and SDBM, respectively). (3) Most samples labeled Py2 (grains in quartz-sulfide-ankerite veinlets) are also classified as orogenic (70% and 78% for SVM and SDBM, respectively). In summary, SVM and SDBM yield *similar results*: Py1b and Py2 samples are classified as orogenic class; Py1a samples, however, exhibit ambiguity between Carlin, orogenic, and sedimentary types. The decision map tends to classify Py1a samples as sedimentary more than the SVM.

Focusing on the decision map (Fig. 4), Py1b and Py2 samples are mainly plotted in the orogenic zone, as expected. However, intriguingly, Py1a samples are divided into two clusters. One cluster is within the orogenic domain, while the other is located around the boundaries of the orogenic, Carlin, and sedimentary zones. From the geological perspective, this bifurcation suggests that the first cluster may have interacted with ore fluids, resulting in a distinct geochemical signature. Consequently, their intricate geochemical features make these data to be a challenge to be classified. As a result, they landed near the decision boundaries of several related decision zones, which are areas of low confidence from the perspective of machine learning classification.

In summary, decision maps offer two significant pieces of additional information beyond mere agreement with the classifier: First, they reveal data *clusters*, which are crucial for interpreting the data, as demonstrated above; Second, the decision maps demonstrate information for *each individual sample*, not as an aggregate score. This includes the level of classification *confidence*, for example, whether a sample is close to a decision boundary. Such detailed information offers a more granular understanding than an overall and general aggregate score.

Exploratory data analyses and model explanation using decision maps

Feature Inverse Projection. The decision maps shown so far are useful to show how all samples spread over the decision zones inferred by the trained model and also allow interpretation of the classification *confidence* in terms of the distance from a sample to its closest decision boundary in the map. However, they do not show which *features* are most responsible for the emergence of the respective decision zones. Understanding this is essential to further explain the studied phenomenon. To address this goal, we propose a new visualization called *feature inverse projection*.

To see the relationship between each feature and the decision zones/boundaries, we created a corresponding map to each feature (pyrite trace elements). For the map of each feature j, $j \in$ {Co, Ni, Cu, Zn, Se, As, Ag, Sb, Au, Bi, Pb}, each pixel p was colored by T^{-1} $(P^{-1}(\mathbf{p})^{j})$, which is the value of the respective feature j, where $T^{-1}(t) = 10^{t} - 1$ is the inverse function of the power transformation given by Equation 4.

Ranking the features. To better guide a better reading of the maps, we propose to rank the features quantitatively. While there are multiple ways to rank the features based on their importance, here we suggest two options: (1) permutation feature importance (Breiman, 2001) for global ranking (all classes), and (2) mutual information (Ross 2014) for local ranking (user selected class).

The permutation feature importance of the classifier gives an intuition of the importance ranking of these trace elements in pyrite genetic type classification globally. The rank of the permutation feature importance of the SVM classifier on the test set is Ni > Au > Sb > Pb > As > Se > Co > Bi > Cu > Ag > Zn (Fig. 5a). The importance value of each feature is the decrease in SVM accuracy on D_T when a single feature value is randomly shuffled. All the importance scores are above zero, which means that all these trace elements are helpful in the classification.

The permutation importance provides a glimpse of the overall feature ranking. However, when the users are interested in how much a feature helps with distinguishing a certain class from all the others, a better option is to design an algorithm to rank for this specific class. Therefore, we tailor mutual information to our decision map case. For each feature j, we calculate the mutual information $I(S_c(f(P^{-1}(\mathbf{p}))), P^{-1}(\mathbf{p})^j)$ for all pixel **p**, where S_c is a function that masks off all labels which are not c (the class label selected by users). Mutual information is a non-negative value. Simply put, it measures the dependence of the feature j and the user-selected class c. It equals 0 if feature j and label c are independent. The higher the value, the stronger the dependency, and thus the visual pattern of the feature aligns better with selected decision zone c and its decision boundaries (discussed below). This quantitative measurement is particularly useful when multiple features show similar patterns.

Note that the ranking methods are to provide the users (geologists) with clues for exploring the data. Geologists' knowledge is still crucial in interpreting the data in this human-centered application case.

Visualizing feature patterns. The resulting inverse projected features are displayed in the permutation importance order (Fig. 5b-l). Black lines in these images show the decision boundaries. Actual feature values of the high-dimensional samples corresponding to every pixel are color-coded on an ordinal colormap (blue=low, red=high feature values). We used a banded colormap having a small number of discrete levels. This way, color changes in the images indicate the actual isolines (equal-feature-value contours) of the respective features in the data. Simply put, if a color band created by the above colormap for value *v* of feature *f* has a shape that matches well the shape of a decision zone for class *c* it is plotted over, it means that the value *v* of *f* is a strong predictor of class *c*. Conversely, if *all* color bands of feature *f* have shapes that do not match well *any* of the decision zones, it means that *f* is not a strongly useful feature for the classification. This can be exemplified by either permutation importance or mutual information ranking: (1) Ni, which is ranked as the most important feature for prediction, shows three color bands (dark blue, light blue, red) which match quite well the Porphyry, VHMS, and Ni-Cu-PGE zones, respectively (Fig. 5b). In contrast, Zn, the least important feature for prediction, shows color bands that match far less well than any of the six decision zones (Fig 5l). While permutation importance gives us an initial understanding of feature relevance, mutual information can provide a more nuanced view, especially in terms of how specific features align with a certain class. (2) For instance, in mutual information ranking, the features with the highest and lowest scores for the orogenic class are Pb and Au, respectively (Fig. 6). The isolines of Pb align well with the shape of the orogenic decision zone (Fig 5e), highlighting Pb is a strong indicator for predicting orogenic class. Conversely, the isolines of Au, being roughly perpendicular to the orogenic decision zone (Fig. 5c), indicate that Au is less useful for discriminating this class.

Let us explore in detail how the feature inverse maps show the relationships between pyrite trace elements and their forming environment types learned from the model. We consider both visual patterns (relations between color bands and decision zones) and feature ranking. We do this in order of permutation importance: (1) The color bands show that Ni > 1000 ppm can distinguish Ni-Cu-PGE from other classes, and Ni < 1 ppm can distinguish porphyry from other classes (Fig. 5b); Mutual information feature ranking confirms the importance of Ni for both Ni-Cu-PGE and porphyry classes (Fig. 6). (2) Au > 100 ppm characterizes pyrites from orogenic and Carlin-type deposits. Au < 0.1 ppm is the character of pyrites from barren sedimentary and Ni-Cu-PGE (magmatic) deposits (Fig. 5c); However, Au is not a strong predictor for any single class, as indicated by its lower mutual information scores (Fig. 6). (3) Pyrite with Sb < 0.1 ppm is more likely from Ni-Cu-PGE or porphyry deposits, while pyrite with Sb > 10 ppm is more likely from the other four classes (Fig. 5d); The mutual information score robustly supports the visual pattern indicating the importance of Sb for the porphyry class (Fig. 6). (4) Pyrites from VHMS deposits, sedimentary and Carlin-type deposits tend to have Pb values > 100 ppm (Fig. 5e); Moreover, as mentioned above, the color band of Pb concentration ranging 10 - 100 ppm aligns well with the shape of the orogenic decision zone, the significance of which is also confirmed by mutual information score for orogenic class (Fig.6). (5) Pyrite from Carlin, orogenic and VHMS deposits have high As values. Most Carlin pyrite and some orogenic pyrite could have As > 10000 ppm (Fig. 5f); When focusing on a single class, As appears to be an efficient predictor for only Carlin class (Fig. 6). (6) Pyrites with Se < 10 ppm are more likely to be from porphyry or orogenic deposits (Fig. 5g); Se, however, does not have a significant mutual information score for distinguishing any single class, as shown in Figure 6. (7) Co > 1000 ppm characterizes Ni-Cu-PGE pyrite (Fig. 5h); Figure 6 highlights Co as the most significant element for the Ni-Cu-PGE class. (8) VHMS and part of the Ni-Cu-PGE zone have Bi > 10 ppm (Fig. 5i); However, Bi's insignificance for single-class discrimination is evident in Figure 6. (9) Cu < 10 ppm is the character of porphyry pyrite. Pyrites in the other four classes have Cu varying from 10 to 10000 ppm (Fig. 5j); The significance of Cu for identifying porphyry class is also strongly confirmed by the mutual information score (Fig.6) (10) The color band of Ag < 1 ppm fairly align with the porphyry zone(Fig. 5k); However, similar to Au, Ag is overall also not efficient for identifying any class, as it never ranks in the top 3 for any class in mutual information score (Fig. 6). (11) The Zn value color bands do not match the decision zones well, except for the band of Zn > 100 ppm, which matches the VHMS zone fairly well (Fig. 5l); And Zn is indeed the most efficient element for distinguishing VHMS from other classes according to mutual information score for VHMS class (Fig.6).

This is the peer-reviewed, final accepted version for American Mineralogist, published by the Mineralogical Society of America.
The published version is subject to change. Cite as Authors (Year) Title. American Mineralogist, in press.
DOI: https://doi.org/10.2138/am-2023-9254. http://www.minsocam.org/

Discussion

Interpretability and limitations of decision maps

Based on the evaluation metrics (Equations 1-3), we established the optimal decision map for the pyrite genetic type classification task. As shown in the results, the SVM has an ACC_C of 0.91, while the decision map for the aforementioned SVM has an ACC_M of 0.88 and a *Cons* of 0.90, on the test set D_T. This means that decision maps can be used to accurately predict how a classifier works. From a visual perspective, there is only a slight overlap of data points in the center of the map (Fig. 2), a property with which no existing 2D discriminant diagram can compete.

Decision maps provide a novel way to get insight into how machine learning classifiers work and where each data point lands in the context of decision boundaries. They should not be seen as a replacement, but rather an enhancement, of traditional classifier metrics (e.g., accuracy): Classifier metrics give a highly *aggregated* quality score (for the entire problem or per class), but do not tell how specific *instances* (train, test, or new) get classified. This is exactly the addition that decision maps provide. More specifically, the actual *shapes* of the decision zones and the spread of instances over them tell how easy is for a given classifier to handle a given data distribution, e.g., which classes are easily separable from the others and/or which parts of the data distribution are easily classifiable.

DOI: https://doi.org/10.2138/am-2023-9254. http://www.minsocam.org/

On top of the samples being categorized into a major class label, Decision maps show how samples are similar to certain other classes via their distances to the closest decision boundaries. Samples near decision boundaries are more uncertain about the predicted label and thus more likely to be misclassified. Feature inverse maps (discussed below) provide additional insights into why these samples may have such problems. However, all these tools need to be complemented by an expert's knowledge to lead to effective interpretations and understanding of the studied phenomenon. Decision maps provide thus a way to combine human knowledge with machine learning predictions when interpreting classification results in a way that cannot be obtained from regular machine learning classification routines. The application of the decision map on the Zaozigou pyrite data discussed next further illustrates the added-value of our visualizations (detailed in the next subsection).

Besides *observation-centric* interpretation (seeing how samples spread with respect to each other and the inferred decision zones), our new addition to decision maps – the feature inverse projections – provides a *class-centric* interpretation, i.e., allows analysts to understand which features and feature values are key responsible for the appearance of specific decision zones or even separate sample groups. These feature inverse projections can be seen as a summary of real-world complex data that show what the model learned and how it decides when values vary. We further discuss this in the next subsection.

Our visual analysis techniques scale well with both the number of samples and the number of dimensions. As shown in Figure 7, the computation time of SDBM is minimally affected by changes in either the number of dimensions or the number of samples. It consistently remains at approximately 3-10 seconds on a standard desktop computer with a consumer-level graphics card. This contrast is particularly noticeable when compared to machine learning classifiers such as SVM, LDA, and QDA, which can be highly sensitive to changes in data dimensionality (Fig. 7). In general, using SDBM to obtain a decision map for a given classifier requires only a few additional seconds after the classifier is trained. Every sample point is reduced to a single 2D scatterplot point. While overplotting does occur, this does not affect, we argue, the usability of our proposal. Indeed, in most applications, one is interested in reasoning about *groups* of similar samples and not every single individual. Such groups become actually better visible when large amounts of samples are plotted. Decision maps also inherit by construction the scalability of the underlying projection techniques to tens or even hundreds of dimensions. Feature inverse projections are less scalable in this sense since we need to plot (and study) one map per feature. However, as discussed above, such maps can be ordered by feature ranking methods (e.g. permutation feature importance, mutual information), so that analysts can focus on a small set of most relevant features. Similar techniques have been used for explaining projections of high-dimensional data for 3D projections (Coimbra et al., 2016).

Decision maps and their proposed extensions are also generically deployable and easy to use: They can be computed fully automatically given *any* trained classifier and *any* datasets (training, test, new) of interest. Exploring the created visualizations also does not require any complex interaction from the user except the optional brushing of points to show details in a tooltip. While the standard implementation of SDBM (Oliveira et al., 2022) does not provide this feature, adding it is very simple. Note that this functionality can target both *existing* points from the projected dataset D used to construct the SDBM, and more interestingly, *new* points that correspond to pixels in the decision map to which no actual data point projects. These effectively generate new, unseen, data points in the high-dimensional space (via the inverse projection P^{-1}) which allow the analyst to reason about how the classifier, or more generally phenomenon under study, would behave for data outside the actually measured dataset one has.

However, decision maps also have some limitations. As explained earlier, both direct and inverse projections have inevitable errors which cannot be fully eliminated in the generic case. We address this issue by quantifying the magnitude of errors and demonstrating that, for classifier analysis, these errors are minimal and do not significantly impact the interpretability of the decision maps. If desired, one can easily extend our proposal by visualizing errors locally in the decision maps following Espadoto et al. (2021). Studying how such more refined error views can help interpret classifiers is an important future work topic. A separate limitation of decision maps is that they do not *explicitly* depict individual dimensions along the two axes of the map, unlike classical discrimination diagrams. Combined with the nonlinear nature of the projections used to create the maps, this asks analysts to deploy more effort to understand how dimensions vary across the map. For example, the pyrite decision zones in Fig. 2 show a trend from the high-temperature forming environment to the low-temperature forming environment in sequence: Ni-Cu-PGE – Porphyry – Orogenic – Carlin. The feature inverse projections help this analysis by mapping the feature variations, one by one, to the respective maps. An interesting future work direction is to summarize several such feature inverse projection images in a single map, thereby reducing the number of different visualizations one needs to study to interpret a decision map.

Implications for mineral deposit genesis classification studies

The dataset used in our work includes Carlin-type pyrite and Ni-Cu-PGE pyrite trace elements, which fills the gap of previous pyrite machine learning related work (Gregory et al., 2019; Zhong et al., 2021). This dataset provides a more comprehensive view of pyrite from magmatic to hydrothermal origins. More importantly, we present a solution to the current problem of the lack of visual interpretability of machine learning in geochemical data classification work. Visual interpretability is a valuable property of traditional geochemistry discriminant diagrams, and it is also a desire for geochemistry data exploration and analysis. Our decision maps solution provides a unique perspective to reveal the structure and properties of data hidden from regular machine learning routines, offering new opportunities for analyzing and explaining geological problems. More specifically, the decision map application on Zaozigou pyrite trace elements shows how *seeing* the data clusters and their locations on the decision map can help interpretation compared to regular machine learning routines; the feature inverse projections application shows how the decision map can uncover what the model learned from the mapping of pyrite trace elements to pyrite forming environments, and displays how the model decides the type of pyrite when the trace element values vary.

We now discuss the specific findings we obtained using decision maps for our specific use-case of studying mineral deposit genesis. Pyrite trace element data of the Zaozigou deposit from Sui et al. (2020) are plotted mainly in the orogenic zone on the decision map. Within this zone, the plotted data clusters are closer to the Carlin and sedimentary zones than the porphyry and Ni-Cu-PGE zones. From the view of pyrite trace elements, Zaozigou shows little similarity to magmatic-related (Ni-Cu-PGE, Porphyry) deposits. Instead, it shows some more similarity to low-temperature Carlin-type deposits. Therefore, it is reasonable that Py1a are plotted around the boundaries of the orogenic zone, Carlin zone, and sedimentary zone (Fig. 4): Since Py1a samples are pyrites in sedimentary within the gold deposit district, Py1a shares similarities to pyrite in barren sedimentary geologically; Carlin-type deposits, which were first found in Nevada, USA, are sediment-hosted, disseminated Au deposits. So, they also share some similarities to pyrite in barren sedimentary. Most of the Carlin-type samples in the dataset are from gold deposits near the edge of the Yangtze craton, in southeast China. These deposits are also argued to be epizonal orogenic gold deposits (Bodnar et al., 2014). If we regard the Carlin class as an epizonal orogenic class, Py1a pyrites are more similar to pyrite from epizonal orogenic deposits than from classic orogenic deposits; Pyrites from Py1b and Py2 are more similar to pyrites from classic orogenic deposits. The conclusion from pyrite trace elements and the decision map method closely agrees with the monazite geochronology conclusion from Qiu et al. (2020).

According to the feature inverse projections (Fig. 5, Fig. 6), some trace elements can be considered indicator elements in discriminating the mineral-forming environments. For example, the model learned that Co, Ni, and Pb are efficient features when classifying Ni-Cu-PGE from others. This model learned knowledge is consistent with geologists' experience that Co, Ni, and their ratio in pyrite are considered reliable indicators and geochemical tools in ore deposit genesis (Bajwah et al., 1987; Bralia et al., 1979). Knowing what the model learned for classifying the pyrite genetic types makes it easy to find other elements as indicators. For example, Pb, which is less discussed in the literature, could be an indicator for discriminating Ni-Cu-PGE, porphyry, and orogenic pyrites from the other classes. In Figure 5, we can observe that the model considers pyrites of Ni-Cu-PGE and porphyry classes to have the feature that Pb < 10 ppm, while orogenic pyrite has Pb roughly between 10 to 100 ppm; Cu could be another indicator for discriminating porphyry pyrite from the other classes, i.e., the model considers porphyry pyrite has the feature that Cu < 10 ppm (Fig. 5j). The effectiveness of Pb and Cu as indicators remains to be further proven in practice.

Implications

The union of information visualization and mineralogy, as presented in this study, heralds a transformative era in geoscience research. By harnessing the capabilities of enhanced decision maps, we have illuminated a novel approach to interpret classification models, deepening our comprehension of multifaceted geochemistry data dimensions.

The introduction of inverse projections is particularly groundbreaking for geology. This feature unravels the depth of understanding models extracting from complex geochemical data, enabling researchers to directly correlate predictions with specific mineralogical features or value-ranges. In the realm of mineral geochemical discrimination, this research signifies a monumental shift. Transitioning from traditional machine learning classification to the advanced visual analytics of machine learning, we're effectively merging the precision and scalability of modern computational methods with the rich, interpretative legacy of discriminant diagrams.

As it continues to lean into data-driven methodologies, our work offers a robust toolset for enhanced mineral genesis classification and exploration. Beyond the immediate applications, this study promises to influence a range of geochemistry sub-disciplines, driving more informed, nuanced, and efficient research and exploration endeavors in the future.

Acknowledgments

This research was financially supported by the National Natural Science Foundation (42261134535, 42072087 and 42130801), the National Key Research Program (2023YFE0125000), the Frontiers Science Center for Deep-time Digital Earth (2652023001), the 111 Project (BP0719021), the Shandong Provincial Engineering Laboratory of Application and Development of Big Data for Deep Gold Exploration (264209), and the China Scholarship Council (202206400020).

References

Bajwah, Z. U., Seccombe, P. K., & Offler, R. (1987). Trace element distribution, Co:Ni ratios and genesis of the big cadia iron-copper deposit, new south wales, australia. *Mineralium Deposita*, *22*(4), 292–300. doi:10/ddmwdr

Belousov, I., Large, R. R., Meffre, S., Danyushevsky, L. V., Steadman, J., & Beardsmore, T. (2016). Pyrite compositions from VHMS and orogenic Au deposits in the Yilgarn Craton, Western Australia: Implications for gold and copper exploration. Ore Geology Reviews, 79, 474–499. doi:10.1016/j.oregeorev.2016.04.020

Belousova, E. A., Griffin, W. L., O'Reilly, S. Y., & Fisher, N. I. (2002a). Apatite as an indicator mineral for mineral exploration: Trace-element compositions and their relationship to host rock type. *Journal of Geochemical Exploration*, *76*(1), 45–69. doi: 10.1016/S0375-6742(02)00204-2

Belousova, E. A., Griffin, W. L., O'Reilly, S. Y., & Fisher, N. L. (2002b). Igneous zircon: Trace element composition as an indicator of source rock type. *Contributions to mineralogy and petrology*, *143*(5), 602–622. doi: 10.1007/s00410-002-0364-7

Bergen, K. J., Johnson, P. A., de Hoop, M. V., & Beroza, G. C. (2019).Machine learning for data-driven discovery in solid Earth geoscience. Science, 363(6433), eaau0323. doi: 10.1126/science.aau0323

Bodnar, R., Lecumberri-Sanchez, P., Moncada, D., & Steele-MacInnis, M. (2014). 13.5 - Fluid Inclusions in Hydrothermal Ore Deposits. In H. D. Holland & K. K. Turekian (Eds.), *Treatise on Geochemistry (Second Edition)* (pp. 119–142). Oxford: Elsevier. doi: 10.1016/B978-0-08-095975-7 .01105-0

Bralia, A., Sabatini, G., & Troja, F. (1979). A revaluation of the Co/Ni ratio in pyrite as geochemical tool in ore genesis problems. *Mineralium Deposita*, *14*(3), 353–374. doi: 10/cr8kvg

Breiman, L. (2001). Random Forests. *Machine learning*, *45*(1), 5–32. doi: 10.1023/a:1010933404324

Breiter, K., Duriˇsov´a, J., & Dosbaba, M.ˇ (2020). Chemical signature of quartz from S-and A-type rare-metal granites–A summary. *Ore Geology Reviews*, *125*, 103674. doi: 10.1016/j.oregeorev.2020.103674

Carvalho, Diogo V., Eduardo M. Pereira, and Jaime S. Cardoso. "Machine learning interpretability: A survey on methods and metrics." Electronics 8.8 (2019): 832.

Chawla, N. V., Bowyer, K. W., Hall, L. O., & Kegelmeyer, W. P. (2002). SMOTE: Synthetic Minority Over-sampling Technique. *Journal of Artificial Intelligence Research*, *16*, 321–357. doi: 10.1613/jair.953

Coimbra, D. B., Martins, R. M., Neves, T. T., Telea, A. C., & Paulovich, F. V. (2016). Explaining three-dimensional dimensionality reduction plots. *Information Visualization*, *15*(2), 154–172. doi: 10.1177/1473871615600010

Cortes, C., & Vapnik, V. (1995). Support-vector networks. *Machine learning*, *20*(3), 273–297.

Cox, D. R. (1958). Two further applications of a model for binary regression. *Biometrika*, *45*(3/4), 562–565.

Chew, D. M., Donelick, R. A., & Sylvester, P. (2012). Combined apatite fission track and U-Pb dating by LA-ICP-MS and its application in apatite provenance analysis. Quantitative Mineralogy and Microanalysis of Sediments and Sedimentary Rocks: Mineralogical Association of Canada, Short Course, 42, 219-247.

Deditius, A. P., Reich, M., Kesler, S. E., Utsunomiya, S., Chryssoulis, S. L., Walshe, J., & Ewing, R. C. (2014). The coupled geochemistry of Au and As in pyrite from hydrothermal ore deposits. *Geochimica et Cosmochimica Acta*, *140*, 644–670. doi: 10/f6h2g4

Deng, J., Qiu, K.F., Wang, Q.F., Goldfarb, R.J., Yang, L.Q., Zi, J.W., Geng, J.Z., Ma, Y., (2020a). In-situ dating of hydrothermal monazite and implications on the geodynamic controls of ore formation in the Jiaodong gold province, Eastern China. Economic Geology, 115(3): 671–685

Deng, J., and Wang, Q.F., (2016). Gold mineralization in China: Metallogenic provinces, deposit types and tectonic framework. Gondwana Research, v. 36, p. 219-274.

Deng, J., Yang, L.Q., Groves, D.I., Zhang, L., Qiu, K.F., Wang, Q.F., (2020b), An integrated mineral system model for the gold deposits of the giant Jiaodong province, eastern China. Earth-Science Reviews, 208:103274

Espadoto, M., Appleby, G., Suh, A., Cashman, D., Li, M., Scheidegger, C. E., Telea, A. C. (2021). UnProjection: Leveraging Inverse-Projections for Visual Analytics of High-Dimensional Data. *IEEE Transactions on Visualization and Computer Graphics*, 1–1. Doi: 10.1109/TVCG.2021.3125576

Espadoto, M., Hirata, N., & Telea, A. (2021). Self-supervised Dimensionality Reduction with Neural Networks and Pseudo-labeling. In *Proceedings of the 16th International Joint Conference on Computer Vision, Imaging and Computer Graphics Theory and Applications – IVAPP,* (pp. 27–37). SciTePress. Doi: 10.5220/0010184800270037

Gregory, D. D., Cracknell, M. J., Large, R. R., McGoldrick, P., Kuhn, S., Maslennikov, V. V., … Lyons, T. W. (2019). Distinguishing Ore Deposit Type and Barren Sedimentary Pyrite Using Laser Ablation-

Inductively Coupled Plasma-Mass Spectrometry Trace Element Data and Statistical Analysis of Large Data Sets. *Economic Geology*, *114*(4), 771. doi: 10.5382/econgeo.4654

He, X., Su, W., Shen, N., Xia, X., & Wang, F. (2021). In situ multiple sulfur isotopes and chemistry of pyrite support a sedimentary source-rock model for the Linwang Carlin-type gold deposit in the Youjiang basin, southwest China. *Ore Geology Reviews*, *139*, 104533. doi: 10.1016/j.oregeorev.2021.104533

Hong, T., Xu, X.-W., Gao, J., Peters, S. G., Li, J., Cao, M., ... You, J. (2018). Element migration of pyrites during ductile deformation of the Yuleken porphyry Cu deposit (NW-China). *Ore Geology Reviews*, *100*, 205– 219. doi: 10.1016/j.oregeorev.2017.10.019

Hou, Z.L., Qiu, K.F., Zhou, T., Cai, Y.W., (2024), An Advanced Image Processin g Technique for Backscatter- Electron Data by Scanning Electron Microscopy for Microscale Rock Exploration. Journal of Earth Science, 35(1): 301– 305. https://doi.org/ 10.1007/s12583-024-1969-9.

Hu, B., L.-P., Liao, W., Wen, G., Hu, H., Li, M. Y. H., & Zhao, X.-F. (2022). The Origin and Discrimination of High-Ti Magnetite in Magmatic-Hydrothermal Systems: Insight from Machine learning Analysis. *Economic Geology*. doi: 10/gqt2bq

Karpatne, A., Ebert-Uphoff, I., Ravela, S., Babaie, H. A., & Kumar, V. (2019). Machine learning for the Geosciences: Challenges and Opportunities.

IEEE Transactions on Knowledge and Data Engineering, *31*(8), 1544–1554. doi: 10.1109/TKDE.2018.2861006

Keith, M., Haase, K. M., Chivas, A. R., & Klemd, R. (2022). Phase separation and fluid mixing revealed by trace element signatures in pyrite from porphyry systems. *Geochimica et Cosmochimica Acta*, *329*, 185–205. doi:10.1016/j.gca.2022.05.015

Large, R. R., Danyushevsky, L., Hollit, C., Maslennikov, V., Meffre, S., Gilbert, S., Foster, J. (2009). Gold and Trace Element Zonation in Pyrite Using a Laser Imaging Technique: Implications for the Timing of Gold in Orogenic and Carlin-Style Sediment-Hosted Deposits. *Economic Geology*, *104*(5), 635–668. doi: 10.2113/gsecongeo.104.5.635

Li, C., Zhang, Z., Li, W., Wang, Y., Sun, T., & Ripley, E. M. (2015). Geochronology, petrology and Hf–S isotope geochemistry of the newly-discovered Xiarihamu magmatic Ni–Cu sulfide deposit in the Qinghai–Tibet plateau, western China. Lithos, 216, 224-240.

Lipton, Zachary C. "The mythos of model interpretability: In machine learning, the concept of interpretability is both important and slippery." Queue 16.3 (2018): 31-57.

Li, Z.-K., Bi, S.-J., Li, J.-W., Zhang, W., Cooke, D. R., & Selby, D. (2017). Distal Pb-Zn-Ag veins associated with the world-class Donggou porphyry Mo deposit, southern North China craton. *Ore Geology Reviews*, *82*, 232–251. doi: 10.1016/j.oregeorev.2016.12.001

Liang, Q.-L., Xie, Z., Song, X.-Y., Wirth, R., Xia, Y., & Cline, J. (2021). EVOLUTION OF INVISIBLE Au IN ARSENIAN PYRITE IN CARLIN-TYPE Au DEPOSITS. *Economic Geology*, *116*(2), 515–526. doi:10.5382/econgeo.4781

Lin, S., Hu, K., Cao, J., Bai, T., Liu, Y., & Han, S. (2021). An in situ sulfur isotopic investigation of the origin of Carlin-type gold deposits in Youjiang Basin, southwest China. *Ore Geology Reviews*, *134*, 104187. doi: 10.1016/ j.oregeorev.2021.104187

Liu, H., Harris, J., Sherlock, R., Behnia, P., Grunsky, E., Naghizadeh, M., Rubingh, K., Tuba, G., Roots, E., & Hill, G. (2023). Mineral prospectivity mapping using machine learning techniques for gold exploration in the Larder Lake area, Ontario, Canada. *Journal of Geochemical Exploration*, 253, 107279. https://doi.org/10.1016/j.gexplo.2023.107279

Liu, J., Li, W., Zhu, X., Zhou, J.-X., & Yu, H. (2020). Ore genesis of the Late Cretaceous Larong porphyry W-Mo deposit, eastern Tibet: Evidence from in-situ trace elemental and S-Pb isotopic compositions. *Journal of Asian Earth Sciences*, *190*, 104199. doi: 10.1016/j.jseaes.2019.104199

Mansur, E. T., Barnes, S.-J., & Duran, C. J. (2021). An overview of chalcophile element contents of pyrrhotite, pentlandite, chalcopyrite, and pyrite from magmatic Ni-Cu-PGE sulfide deposits. *Mineralium Deposita*, *56*(1), 179–204. doi: 10.1007/s00126-020-01014-3

Mavrogonatos, C., Voudouris, P., Zaccarini, F., Klemme, S., Berndt, J., Tarantola, A., ... Spry, P. (2020). Multi-Stage Introduction of Precious and Critical Metals in Pyrite: A Case Study from the Konos Hill and Pagoni Rachi

Porphyry/Epithermal Prospects, NE Greece. *Minerals*, *10*(9), 784. doi:10.3390/min10090784

Molnar, C. (2020). *Interpretable Machine learning*. Lean Publishing.

Oliveira, A. A., Espadoto, M., Hirata Jr, R., & Telea, A. C. (2022). SDBM: Supervised Decision Boundary Maps for Machine learning Classifiers. In *VISIGRAPP (3: IVAPP)* (pp. 77–87).

O'Sullivan, G., Chew, D., Kenny, G., Henrichs, I., & Mulligan, D. (2020). The trace element composition of apatite and its application to detrital provenance studies. *Earth-Science Reviews*, *201*, 103044. doi: 10.1016/j.earscirev.2019.103044

Pearce, J. A., & Cann, J. R. (1973). Tectonic setting of basic volcanic rocks determined using trace element analyses. *Earth and planetary science letters*, *19*(2), 290–300. doi: 10.1016/0012-821X(73)90129-5

Pedregosa, F., Varoquaux, G., Gramfort, A., Michel, V., Thirion, B., Grisel, O., ... Dubourg, V. (2011). Scikit-learn: Machine learning in Python. *the Journal of machine learning research*, *12*, 2825–2830.

Petrelli, M. (2021). Introduction to Python in Earth Science Data Analysis: From Descriptive Statistics to Machine Learning. Springer International Publishing. https://doi.org/10.1007/978-3-030-78055-5

Petrelli, M., & Perugini, D. (2016). Solving petrological problems through machine learning: The study case of tectonic discrimination using geochemical and isotopic data. *Contributions to Mineralogy and Petrology*, *171*(10), 81. doi: 10.1007/s00410-016-1292-2

Qiu, K.F., Deng, J., He, D.Y., Rosenbaum, G., Zheng, X., Williams-Jones, A.E., Yu, H.C., Balen, D., (2023). Evidence of vertical slab tearing in the Late Triassic Qinling Orogen (central China) from multiproxy geochemical and isotopic imaging. Journal of Geophysical Research: Solid Earth, 128, e2022JB025514.

Qiu, K.F., Deng, J., Yu, H.C., Rasbury, T., Tang, Y.W., Zhu, R., Zhang, P.C., Goldfarb, R., (2024a), The Zaozigou orogenic gold-antimony deposit, West Qinling Orogen, China: Structural controls on multiple mineralization events: Geological Society of America Bulletin, https://doi.org/10.1130/B37029.1.

Qiu, K.F., Romer, R., Long, Z.Y., Yu, H.C., Tumer, S., Wan, R.Q., Li, X.Q., Gao, Z.Y., Deng, J., (2024b). Potassium isotopes as a tracer of hydrothermal alteration in ore systems. Geochimica et Cosmochimica Acta, https://doi.org/10.1016/j.gca.2024.01.005.

Qiu, K. F., Yu, H. C., Deng, J., McIntire, D., Gou, Z. Y., Geng, J. Z., ... Goldfarb, R. (2020). The giant Zaozigou Au-Sb deposit in West Qinling, China: Magmatic-or metamorphic-hydrothermal origin? *Mineralium Deposita*, 1–18

Qiu, K.F., Zhou, T., Chew, D. M., Hou, Z.L., Müller, A., Yu, H.C., Lee, R. H. G., Chen, H., & Deng, J. (2024c). Apatite trace element composition as an indicator of ore deposit types: A machine learning approach. *American Mineralogist*. 109(2), 303-314.

Revan, M. K., Genç, Y., Maslennikov, V. V., Maslennikova, S. P., Large, R. R., & Danyushevsky, L. V. (2014). Mineralogy and trace-element geochemistry of sulfide minerals in hydrothermal chimneys from the

UpperCretaceous VMS deposits of the eastern Pontide orogenic belt (NE Turkey). *Ore Geology Reviews*, *63*, 129–149. doi: 10.1016/j.oregeorev.2014.05.006

Rodrigues, F. C. M., Espadoto, M., Hirata, R., & Telea, A. C. (2019). Constructing and Visualizing High-Quality Classifier Decision Boundary Maps. *Information*, *10*(9), 280. doi: 10.3390/info10090280

Rodrigues, F. C. M., Hirata, R., & Telea, A. C. (2018). Image-based visualization of classifier decision boundaries. In *2018 31st SIBGRAPI Conference on Graphics, Patterns and Images (SIBGRAPI)* (pp. 353–360). IEEE.

Ross, B. C. (2014). Mutual information between discrete and continuous data sets. *PloS one*, 9(2), e87357.

Rottier, B., & Casanova, V. (2020). Trace element composition of quartz from porphyry systems: A tracer of the mineralizing fluid evolution. *Mineralium Deposita*, 1–20.

Rusk, B. (2012). Cathodoluminescent Textures and Trace Elements in Hydrothermal Quartz. In J. G¨otze & R. M¨ockel (Eds.), *Quartz: Deposits, Mineralogy and Analytics* (pp. 307–329). Berlin, Heidelberg: Springer Berlin Heidelberg. doi: 10.1007/978-3-642-22161-3 14

Sheng, Y.-M. (2022). Distal gold mineralization associated with porphyry system: The case of Hongzhuang and Yuanling deposits, East Qinling, China. *Ore Geology Reviews*, 16. doi: 10.1016/j.oregeorev.2022.104701

Sui, J.-X., Li, J.-W., Hofstra, A. H., O'Brien, H., Lahaye, Y., Yan, D., ... Jin, X.Y. (2020). Genesis of the Zaozigou gold deposit, West Qinling orogen, China: Constraints from sulfide trace element and stable isotope geochemistry. Ore Geology Reviews, 122, 103477. doi: 10.1016/j.oregeorev.2020.103477

Tufte, E. R. (1983). The visual display of quantitative information Graphics Press. Cheshire, Connecticut, 6410.

Van der Maaten, L., & Hinton, G. (2008). Visualizing data using t-SNE. Journal of machine learning research, 9(11).

Wang, Y., Machado, A., & Telea, A. (2023). Quantitative and Qualitative Comparison of Decision-Map Techniques for Explaining Classification Models. *Algorithms*, 16(9), 438.

Wang, Y., Qiu, K., Hou, Z., & Yu, H. (2022). Quartz Ti/Ge-P discrimination diagram: A machine learning based approach for deposit classification. *Acta Petrologica Sinica*, 38(1), 281–290. https://doi.org/10.18654/1000-0569/2022.01.18

Wang, Y., Qiu, K., Müller, A., Hou, Z., Zhu, Z., & Yu, H. (2021). Machine Learning Prediction of Quartz Forming-Environments. *Journal of Geophysical Research: Solid Earth*, 126(8), e2021JB021925. https://doi.org/10.1029/2021jb021925

Wilkinson, L., Anand, A., & Grossman, R. (2005). Graph-theoretic scagnostics. In *Information Visualization, IEEE Symposium on* (pp. 21–21). IEEE Computer Society.

Xie, Z., Xia, Y., Cline, J. S., Pribil, M. J., Koenig, A., Tan, Q., ... Yan, J. (2018, November). Magmatic Origin for Sediment-Hosted Au Deposits, Guizhou Province, China: In Situ Chemistry and Sulfur Isotope Composition of

Pyrites, Shuiyindong and Jinfeng Deposits. *Economic Geology*, *113*(7), 1627–1652. doi: 10.5382/econgeo.2018.4607

Yeo, I.-K., & Johnson, R. A. (2000). A new family of power transformations to improve normality or symmetry. *Biometrika*, *87*(4), 954–959. doi: 10.1093/ biomet/87.4.954

Yu, H.C., Qiu, K.F., Deng, J., Zhu, R. Mathieu, L., Sai, S.X., Sha, W. J., (2022a). Ex huming and preserving epizonal orogenic Au-Sb deposits in rapidly uplifting orogenic settings. Tectonics, 41, e202 1TC007165.

Yu, H.C., Qiu, K.F., Pirajno, F., Zhang, P.C., Dong, W.Q., (2022b). Revisiting Pha nerozoic evolution of the Qinling Orogen (East Tethys) with perspect ives of detrital zircon. Gondwana Research, 103: 426-444.

Yuan, J., Chen, C., Yang, W., Liu, M., Xia, J., & Liu, S. (2021). A survey of visual analytics techniques for machine learning. *Computational Visual Media*, *7*(1), 3–36. doi: 10/ghtgx8

Zhong, R., Deng, Y., Li, W., Danyushevsky, L. V., Cracknell, M. J., Belousov, I., ... Li, L. (2021). Revealing the multi-stage ore-forming history of a mineral deposit using pyrite geochemistry and machine learning based data interpretation. *Ore Geology Reviews*, *133*, 104079. doi:10.1016/j.oregeorev.2021.104079

Zhou, H., Müller, A., & Berndt, J. (2023). Quartz chemistry fingerprints melt evolution and metamorphic modifications in high-purity quartz deposits. *Geochimica et Cosmochimica Acta.*

Zhou, T., Qiu, K., Wang, Y., Yu, H., & Hou, Z. (2022). Apatite Eu/Y-Ce discrimination diagram: A big data based approach for provenance classification. *Acta Petrologica Sinica*, 38(1), 291–299. https://doi.org/10.18654/1000-0569/2022.01.19

Zhu, Z., Zhou, F., Wang, Y., Zhou, T., Hou, Z., & Qiu, K. (2022). Machine learning-based approach for zircon classification and genesis determination. *Earth Science Frontiers*, 29(5), 464.

DOI: https://doi.org/10.2138/am-2023-9254. http://www.minsocam.org/

List of figure captions

Figure 1. Workflow of the optimal decision map construction and evaluation. Abbreviation: LR, Logistic Regression; SVM, Support Vector Machine; RF, Random Forest; NN, Neural Network.

Figure 2. Decision Map built from the training set and the trained SVM. Training set samples are plotted as colored dots without outlines. Test set samples are plotted as colored dots with black outlines. Darker pixels in the map (mainly pixels close to the decision boundaries) show lower classification confidence.

Figure 3. (a) Confusion matrix for the actual SVM classifier. (b) Confusion matrix for the trained decision map for this classifier.

Figure 4. Zaozigou pyrite trace element data plotted on the trained decision map. The pyrite trace element data is from Sui et al. (2020).

Figure 5. (a) Permutation feature importance of the SVM classifier. (b-l) Feature inverse projections for all the 11 features of the considered dataset that explain which features and feature-values are most responsible for the appearance of the learned decision zones.

Figure 6. Mutual information scores ranking feature importance for each class respectively.

Figure 7. Plot showing the time taken by SDBM and 5 common classifiers, utilizing synthetic datasets of varying dimensionality and number of samples (n_samples). The time recorded for SDBM includes the duration for fitting training samples and inverse projecting grids (grid size: 300^2); whereas, for classifiers, it records the time for fitting and predicting labels for the training samples. Abbreviation: RF, Random Forest; SVM, Support Vector Machine NN, Neural Network; LDA, Linear Discriminant Analysis; QDA, Quadratic Discriminant Analysis.

DOI: https://doi.org/10.2138/am-2023-9254. http://www.minsocam.org/

Appendix

The data and source codes to reproduce this work are available for download at the link: https://github.com/wuyuyu1024/SDBM_for_Pyrite (accessed on Feb. 18 2024).

Tables

Table 1. Published pyrite trace element datasets used in this study.

Class	No. of samples	References
Ni-Cu-PGE	263	(Mansur et al., 2021)
Porphyry	658	(Hong et al., 2018; Keith et al., 2022; Li et al., 2017; Liu et al., 2020; Mavrogonatos et al., 2020; Sheng, 2022)
Orogenic	615	(Zhong et al., 2021)
Carlin	487	(He et al., 2021; Large et al., 2009; Liang et al., 2021; Lin et al., 2021; Xie et al., 2018)
VHMS	150	(Revan et al., 2014; Zhong et al., 2021)
Sedimentary	1421	(Zhong et al., 2021)

Table 2. Search results of the classifiers for building the Decision Boundary Map. The highest value per metric type is indicated in bold.

Model	Classifier accuracy ACC_C	Map accuracy ACC_M	Consistency *Cons*
Logistic Regression	0.855176	0.917917	0.870568
Support Vector Machine (SVM)	0.942248	**0.925539**	**0.922167**
Random Forest	**0.984317**	0.885665	0.885665
Neural Network	0.977870	0.874088	0.875261

Table 3. Zaozigou pyrite trace element data classification result from the SVM

	Ni-Cu-PGE	Porphyry	Orogenic	Carlin	VMS	Sedimentary
Py1a	0 (0.00%)	0 (0.00%)	18 (43.90%)	23 (56.10%)	0 (0.00%)	0 (0.00%)
Py1b	0 (0.00%)	0 (0.00%)	30 (93.75%)	2 (6.25%)	0 (0.00%)	0 (0.00%)
Py2	0 (0.00%)	2 (5.41%)	26 (70.27%)	7 (18.92%)	2 (5.41%)	0 (0.00%)
Total	0 (0.00%)	2 (1.82%)	74 (67.27%)	32 (29.09%)	2 (1.82%)	0 (0.00%)

Table 4. Zaozigou pyrite trace element data classification result from the SDBM

	Ni-Cu-PGE	Porphyry	Orogenic	Carlin	VMS	Sedimentary
Py1a	0 (0.00%)	0 (0.00%)	16 (39.02%)	6 (14.63%)	0 (0.00%)	19 (46.34%)
Py1b	0 (0.00%)	2 (6.25%)	27 (84.38%)	2 (6.25%)	0 (0.00%)	1 (3.12%)
Py2	0 (0.00%)	0 (0.00%)	29 (78.38%)	5 (13.51%)	2 (5.41%)	1 (2.70%)
Total	0 (0.00%)	2 (1.82%)	72 (65.45%)	13 (11.82%)	2 (1.82%)	21 (19.09%)

Figure 1

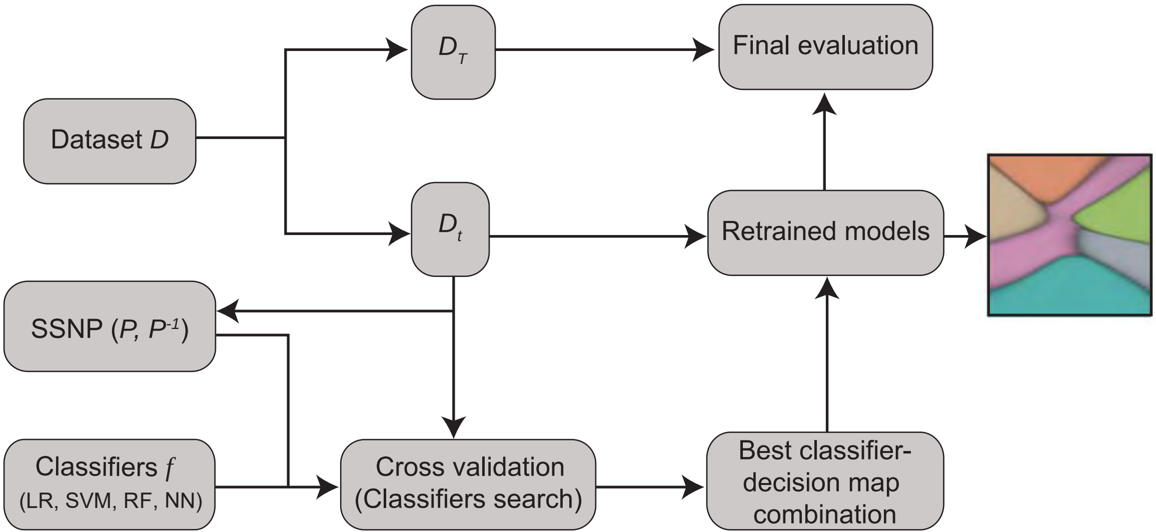
Dataset D
D_T
D_t
Final evaluation
Retrained models
SSNP (P, P^{-1})
Classifiers f
(LR, SVM, RF, NN)
Cross validation
(Classifiers search)
Best classifier-
decision map
combination

Figure 2

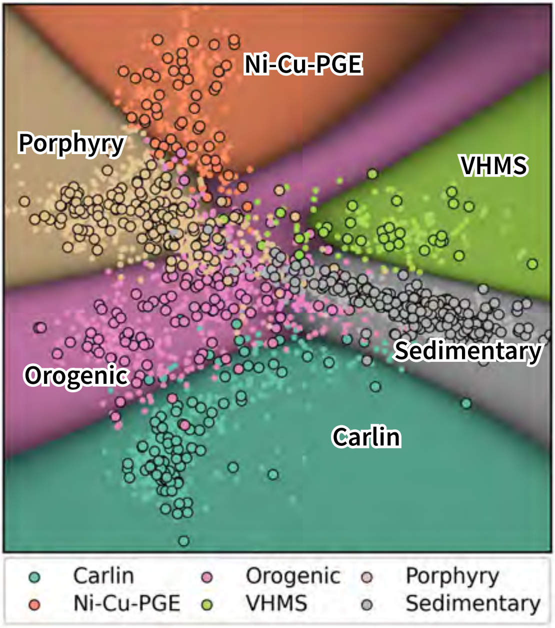
Ni-Cu-PGE
Porphyry
VHMS
Sedimentary
Orogenic
Carlin
Carlin
Orogenic
Porphyry
Ni-Cu-PGE
VHMS
Sedimentary

Figure 3

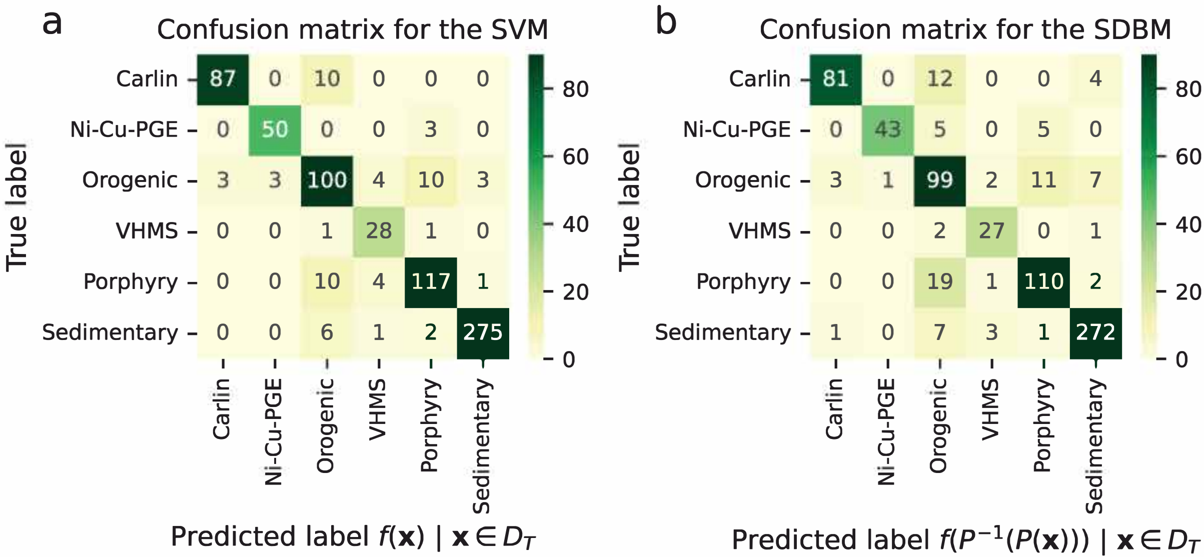

a
Confusion matrix for the SVM
True label
Carlin
Ni-Cu-PGE
Orogenic
VHMS
Porphyry
Sedimentary
87 0 10 0 0 0
0 50 0 0 3 0
3 3 100 4 10 3
0 0 1 28 1 0
0 0 10 4 117 1
0 0 6 1 2 275
80
60
40
20
0
Predicted label $f(\mathbf{x}) \mid \mathbf{x} \in D_T$
b
Confusion matrix for the SDBM
81 0 12 0 0 4
0 43 5 0 5 0
3 1 99 2 11 7
0 0 2 27 0 1
0 0 19 1 110 2
1 0 7 3 1 272
Predicted label $f(P^{-1}(P(\mathbf{x}))) \mid \mathbf{x} \in D_T$

Figure 4

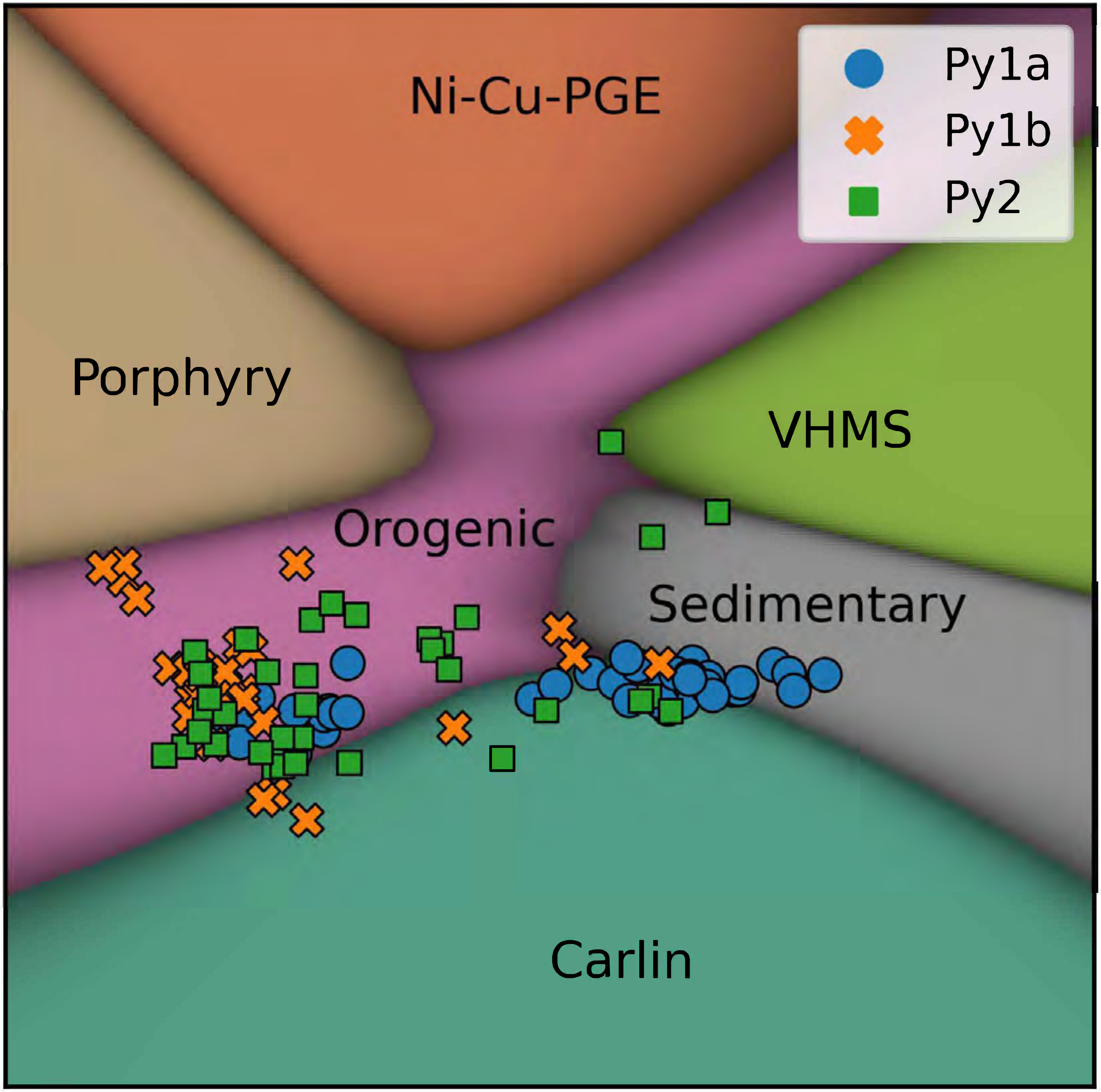
Ni-Cu-PGE
Porphyry
VHMS
Orogenic
Sedimentary
Carlin
Py1a
Py1b
Py2

Figure 5

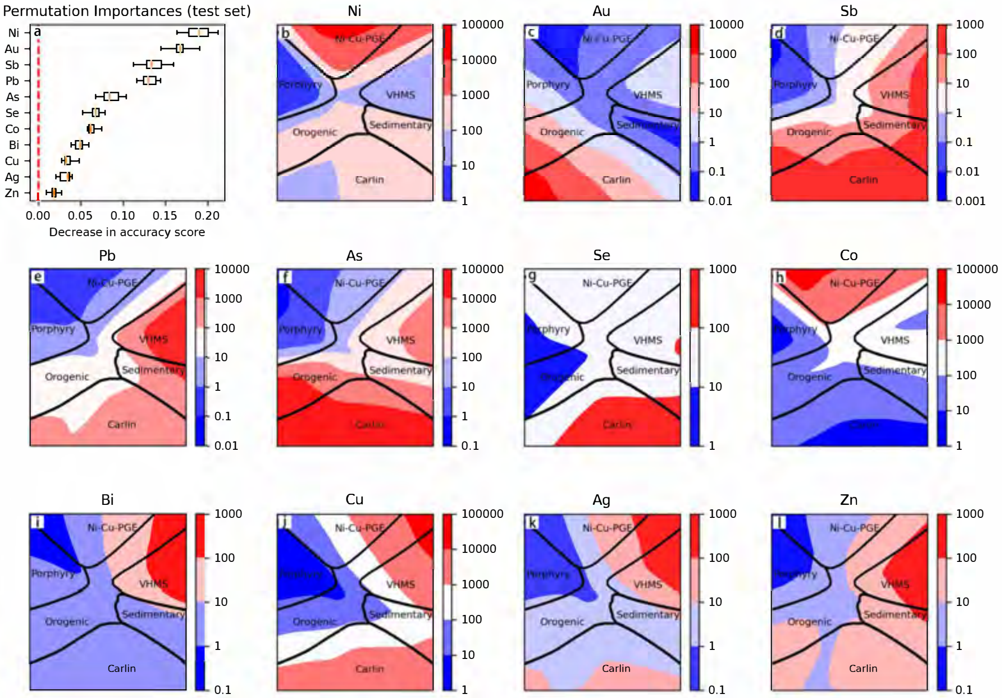

Permutation Importances (test set)
a
Ni
Au
Sb
Pb
As
Se
Co
Bi
Cu
Ag
Zn
0.00
0.05
0.10
0.15
0.20
Decrease in accuracy score
Ni
Au
Sb
Pb
As
Se
Co
Bi
Cu
Ag
Zn
Ni-Cu-PGE
Porphyry
VHMS
Orogenic
Sedimentary
Carlin

Figure 6

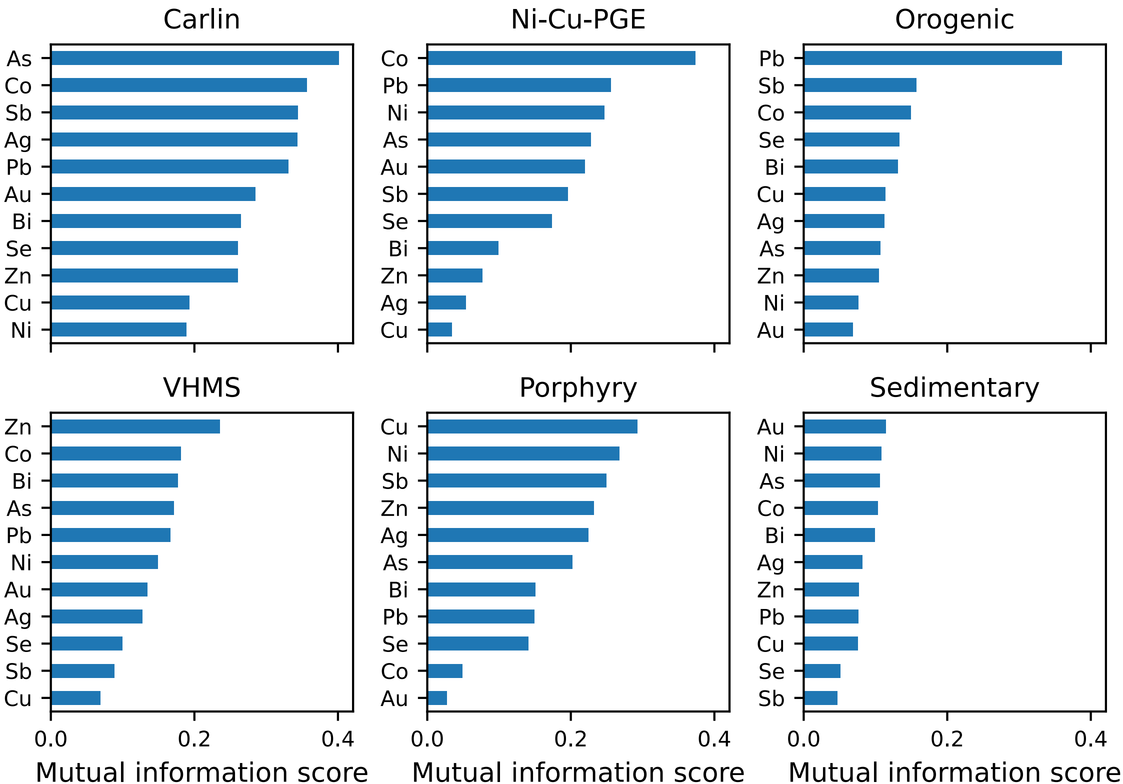

Carlin
As
Co
Sb
Ag
Pb
Au
Bi
Se
Zn
Cu
Ni
Ni-Cu-PGE
Co
Pb
Ni
As
Au
Sb
Se
Bi
Zn
Ag
Cu
Orogenic
Pb
Sb
Co
Se
Bi
Cu
Ag
As
Zn
Ni
Au
VHMS
Zn
Co
Bi
As
Pb
Ni
Au
Ag
Se
Sb
Cu
Porphyry
Cu
Ni
Sb
Zn
Ag
As
Bi
Pb
Se
Co
Au
Sedimentary
Au
Ni
As
Co
Bi
Ag
Zn
Pb
Cu
Se
Sb
0.0
0.2
0.4
Mutual information score

Figure 7

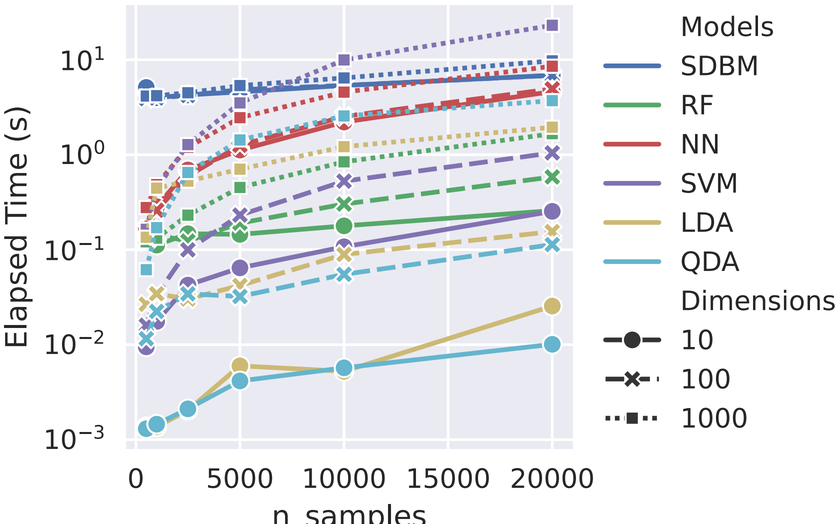
Elapsed Time (s)
10^{1}
10^{0}
10^{-1}
10^{-2}
10^{-3}
0
5000
10000
15000
20000
n_samples
Models
SDBM
RF
NN
SVM
LDA
QDA
Dimensions
10
100
1000